

## Recommendations on dynamic pressure sensor placement for transonic wind tunnel tests

Michael Y. Yang\* and Michael T. Palodichuk

ATA Engineering, Inc. 13290 Evening Creek Drive South, Suite 250, San Diego, California, U.S.A.

(Received September 15, 2018, Revised February 9, 2019, Accepted March 14, 2019)

**Abstract.** A wind tunnel test was conducted that measured surface fluctuating pressures aft of a ramp at transonic speeds. Dynamic pressure test data was used to perform a study to determine best locations for streamwise sensor pairs for shocked and unshocked runs based on minimizing the error in root-mean-square acceleration response of the panel. For unshocked conditions, the upstream sensor is best placed at least 6.5 ramp heights downstream of the ramp, and the downstream sensor should be within 2 ramp heights from the upstream sensor. For shocked conditions, the upstream sensor should be between 1 and 7 ramp heights downstream of the shock, with the downstream sensor 2 to 3 ramp heights of the upstream sensor. The shock was found to prevent the passage coherent flow structures; therefore, it may be desired to use the shock to define the boundary of subzones for the purpose of loads definition. These recommendations should be generally applicable to a range of expansion corner geometries in transonic flow provided similar flow structures exist. The recommendations for shocked runs is more limited, relying on data from a single dataset with the shock located near the forward end of the region of interest.

**Keywords:** wind tunnel testing; shock; vibroacoustics; transonic; dynamic pressure; random; acceleration response

---

### 1. Introduction

Random vibrations in launch vehicles are driven by external fluctuating pressure (or aeroacoustic) environments, and these vibrations, although usually not severe enough to endanger primary structure, are often the design drivers for electronic components such as avionics. These fluctuating pressure loads are most often derived from scale-model wind tunnel testing or scaling of historical data. A typical wind tunnel test is described by Reed *et al.* (2012), who described a wind tunnel test for a rigid scale model of the Ares I-X launch vehicle that utilized dynamic pressure sensors to define the aeroacoustic loading during ascent. Although the vast majority of aeroacoustic wind tunnel tests in the aerospace industry use rigid models, there are some examples where vibration measurements were performed on flexible models. Coe and Chyu (1972) used a moveable wall to position a shock directly on or off a flexible panel. Similar work was performed by Rizzi *et al.* (2000) for window blanks of supersonic aircraft. In the aerospace industry, the fluctuating pressure data collected is typically fit to models such as that proposed by Corcos (1963) and then applied to analysis models to predict random vibration response.

---

\*Corresponding author, Ph.D., E-mail: [michael.yang@ata-e.com](mailto:michael.yang@ata-e.com)

To date, there is very little known published guidance for the precise location of dynamic pressure sensors on scale models of launch vehicles. Budget and space constraints limit the number of sensors placed, and some wind tunnel tests in the aerospace industry may have only a single sensor in a region of interest, despite a minimum of three sensors being required to define a Corcos turbulent boundary layer forcing function. The lack of sensor resolution to fully define the loading becomes more problematic if the flow is inhomogeneous (e.g., contains shocks). Steady computational fluid dynamics (CFD) has traditionally been used to visualize flow regimes. This visualization can be used to aid in the placement of dynamic pressure sensors, but it is insufficient to provide higher-fidelity information regarding ideal sensor spacing. More recently, CFD is being used to directly predict the surface fluctuating pressures. Alter *et al.* (2015) describe the use of delayed detached eddy simulation (DDES) to calculate a transonic flow field about the Space Launch System for up to 1.5 physical seconds. The entire computation took 1595 wall-clock hours. The CFD results were compared against a 2.5% wind tunnel model and showed good agreement.

Yang *et al.* (2017) showed that variations in the location of closely spaced sensor pairs result in large variations in the Corcos parameters of convection velocity and streamwise and spanwise decay coefficients. This could lead to deviations of greater than 10 dB in predicted root-mean-square (RMS) response when the pressure sensor locations are chosen randomly. The same authors used high-resolution measurements of surface fluctuating pressure (SFP) to derive wavenumber- and Corcos-based loading models. These loading models were used to predict the random acceleration response of a flexible panel, which was then correlated to accelerometer measurements of the same panel in the wind tunnel.

This paper utilizes high-resolution dynamic pressure measurements taken downstream of a two-dimensional 45° ramp in transonic flow in air, as described by Yang *et al.* (2017). Acceleration measurements were also taken of a flexible panel in the same location. The pressure array consisted of a large number of closely spaced sensors, which was critical to the wavenumber analysis. However, the use of such an array is impractical for use with scale models of launch vehicles due to budget and space constraints. Yang and Palodichuk (2018) extended the previous work by exploring the range of acceleration responses predicted when a practical number of sensors are used and provides recommendations for sensor placement for future transonic wind tunnel tests. This paper provides more information on the errors in acceleration response that are probable if pressure sensor locations are not chosen properly. For sake of completeness, much of the work discussed in the 2018 paper is described here as well.

The paper begins with a description of the wind tunnel test, with details of the test article, flow conditions, and instrumentation. The next section provides a brief theoretical review showing derivation of Corcos cross-spectral parameters and how panel acceleration power spectral density (PSD) responses are calculated using wavenumber analysis. The methodology used to determine sensor placement is then described, followed by an analysis of vibration prediction errors and recommendations for sensor placement. The paper ends with a brief summary and conclusions.

## 2. Description of wind tunnel test

Wind tunnel testing took place at the National Center for Physical Acoustics (NCPA) at the University of Mississippi (UM). The Tri-Sonic Wind Tunnel (TSWT) is a blow-down tunnel designed for the study of fluid-structure interactions in high-speed flows. The wind tunnel test measured both panel vibrations and SFPs through the use of a pair of geometrically identical test

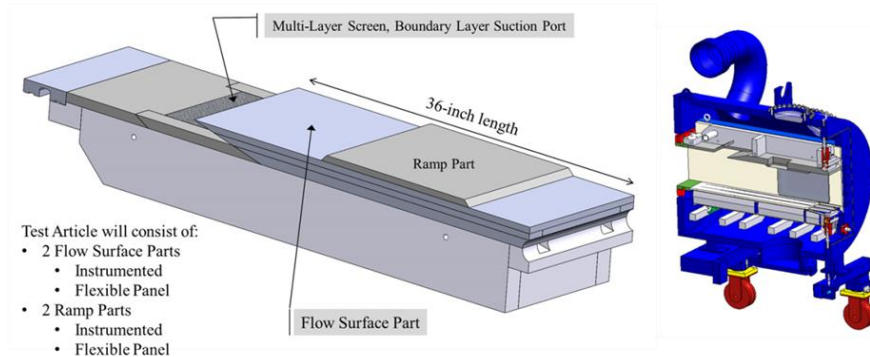


Fig. 1 Test article (left) for insertion into TSWT (right)

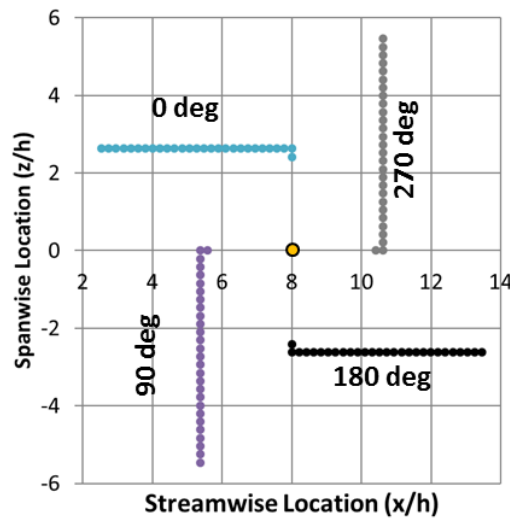


Fig. 2 Conceptual diagram showing pressure sensor locations for all four array orientations. Flow is from left to right

articles, one of which had a rigid ramp part instrumented to measure SFPs, whereas the other had a ramp part containing a flexible panel whose vibration response could be measured. An upstream scoop removed the incoming boundary layer, and the ramp was designed to create an expansion region aft of the ramp. At lower transonic Mach values, this creates a separation bubble just aft of the ramp. At high transonic Mach values, this results in a termination shock aft of the ramp. The region near this shock is also known as the reattachment zone. The ramp is angled at  $45^\circ$  and is  $\frac{3}{8}$ " (9.525 mm) tall. The entire test article was placed in the ceiling of the tunnel's 12" by 12" (304.8 x 304.8 mm) working section. The test article and a cross-section of the working section of the wind tunnel are shown in Fig. 1.

The test article was designed to be modular to allow both surface pressure and panel vibration measurements to be taken with replacement of the ramp part. The flexible panel part consists of a  $\frac{1}{8}$ " (3.175 mm) thick sheet of aluminum epoxied to an aluminum block with a 4" (101.6 mm) by 5" (127 mm) cutout to create a thin panel with well-defined boundary conditions. The pressure

array ramp consists of a square aluminum panel containing the pressure array, which sits inside the solid aluminum ramp.

The flexible panel was instrumented with five PCB 352A25 accelerometers. These accelerometers were chosen for their light weight and high acceleration rating. They have a sensitivity of 2.5 mV/g, a measurement range up to 2000 g peak, and an operating frequency range between 1 and 10000 Hz. They were attached to the panel with epoxy in locations that would allow a reasonable spatial average response to be measured.

The high-resolution pressure sensor array was originally designed for wavenumber analysis, which required the array to have high spatial resolution in addition to measuring pressures over as much of the panel area as possible. The pressure sensor array was mounted in a square plate in an offset L configuration that can be rotated in 90° increments between tunnel runs while all tunnel conditions are kept stationary. There are 27 sensors in the main part of the array, in addition to a single offset sensor and a single sensor in the center of the panel. These sensors were a mix of Kulite XCQ-055 (0.055" or 1.397 mm diameter) and Measurement Specialties EPIH-112 (0.050" or 1.27 mm diameter), with a 2 mm (0.0788") spacing. Fig. 2 shows the locations of the pressure sensors for all four array orientations.

A total of 315 runs were performed at Mach 0.75, 0.80, 0.85, and 0.89. Runs at stagnation pressures of 20, 40, and 60 psia were performed at each Mach number. The Reynolds number per foot ranged between 5.87e6 and 19.0e6. Dynamic data was taken to adequately resolve the range from 500 Hz to 10 kHz. Tunnel runs were used to (1) verify proper function of the boundary layer scoop and tune tunnel controls, (2) ensure that there was no significant spanwise variance in the flow, (3) collect SFP measurements, and (4) collect vibration responses of a flexible panel. A normal shock downstream of the ramp was observed for all Mach 0.85 and 0.89 runs. Murray *et al.* (2017) and Yang *et al.* (2017) provide additional descriptions of the wind tunnel testing program.

### 3. Theoretical background

This section provides a brief description of the Corcos model, how the authors derived its cross-spectral parameters from test data, and how predictions of structural response are made using wavenumber analysis.

#### 3.1 Derivation of Corcos cross-spectral parameters

The cross-spectrum of an aeroacoustic fluctuating pressure field between two points is often described using the Corcos (1963) model, which assumes that the cross-spectrum in the streamwise and cross-stream directions can be separated and that the cross-spectrum decays exponentially. This model was originally developed for homogeneous attached turbulent boundary layers and may not model inhomogeneous turbulent boundary layers very well. However, it is commonly used to define aeroacoustic loads in the aerospace industry, particularly for the ascent phase of launch vehicles. It can be written as

$$G_p(x, z, f) = \widehat{G}_p(f) e^{-k_c \alpha_x x} e^{-k_c \alpha_z z} e^{-ik_c x} \quad (1)$$

The Corcos model has three parameters: the convection velocity (or convection wavenumber,  $k_c$ ), a decay coefficient in the streamwise direction,  $\alpha_x$ , and a decay coefficient in the spanwise

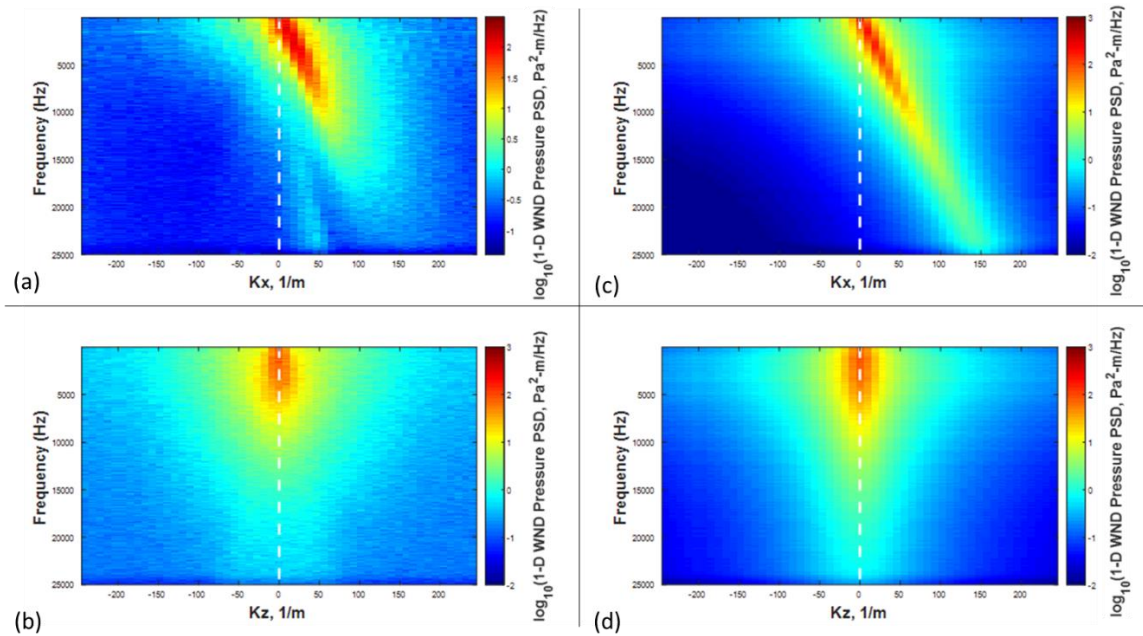


Fig. 3 Comparison of wavenumber-frequency spectra at Mach 0.80, 40.1 psia. (a) Streamwise, direct from test data, (b) spanwise, direct from test data, (c) streamwise, wavenumber model and (d) spanwise, wavenumber model

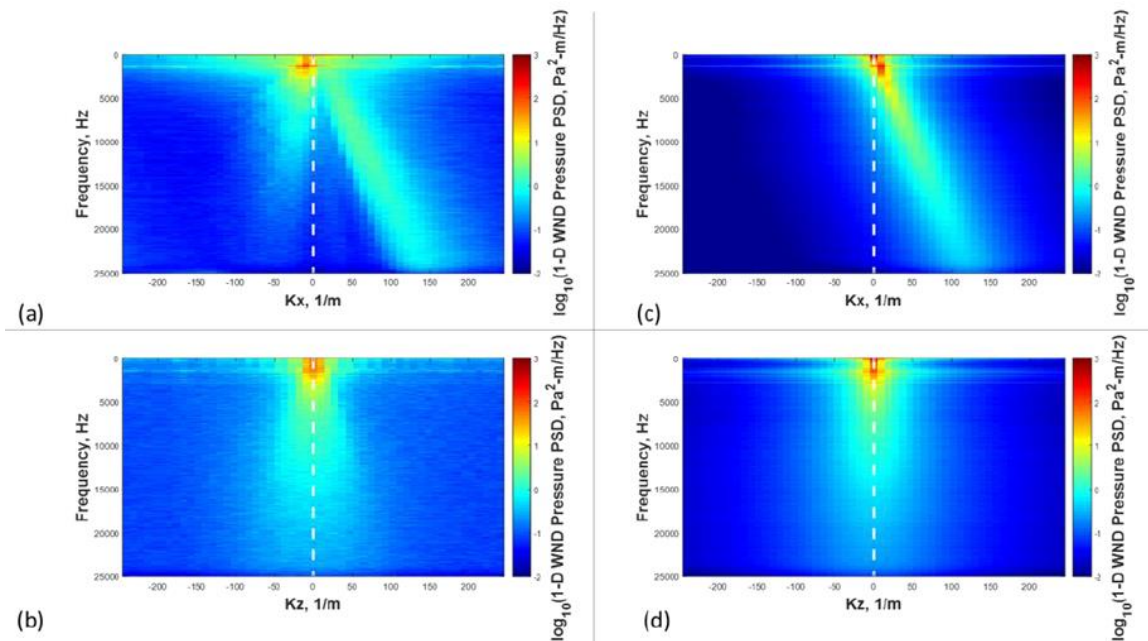


Fig. 4 Comparison of wavenumber-frequency spectra at Mach 0.85, 40.1 psia. (a) Streamwise, direct from test data, (b) spanwise, direct from test data, (c) streamwise, wavenumber model and (d) spanwise, wavenumber model

direction,  $\alpha_z$ . Correspondingly, these three parameters can be estimated from test data using a pair of sensors in the streamwise direction and another pair of sensors in the spanwise direction. Three pressure sensors (at a minimum) can be used to derive the Corcos parameters if the sensors are arranged in an L pattern. The symbol  $\widehat{G}_p$  in Eq. (1) is the spatially averaged pressure autospectrum.

The group velocity is used to estimate convection velocity,  $U_c$ , as shown in Eq. (2), where  $\Delta x$  is the spacing between pressure sensors,  $\Delta f$  is the difference in frequency, and  $\Delta\theta$  is the difference in unwrapped phase. A frequency range that produces an approximately linear dropoff in phase is selected for this calculation, and the convection velocity is assumed to be constant with respect to frequency.

$$U_c = -2\pi\Delta x \frac{\Delta f}{\Delta\theta} = \frac{2\pi f}{k_c} \quad (2)$$

Eqs. (3) and (4) show that the streamwise and spanwise decay coefficients are derived from the coherence,  $\gamma^2$ , between the two sensors, the distance between the sensors, and the convection wavenumber,  $k_c$ . Typically, only frequency ranges where the coherence is greater than 0.1 are used.

$$\alpha_x = \frac{-\ln(\sqrt{\gamma^2})}{k_c\Delta x} \quad (3)$$

$$\alpha_z = \frac{-\ln(\sqrt{\gamma^2})}{k_c\Delta z} \quad (4)$$

A comparison between the wavenumber-frequency spectra derived directly from the test data and the resulting wavenumber-frequency spectra when the Corcos model is used is shown for an unshocked run in Fig. 3. The plot indicates that the Corcos model is a reasonably good fit to the measured pressure data. Additional information on how the Corcos model parameters were derived for this plot is given in Yang *et al.* (2017).

A similar comparison for a shocked run is given in Fig. 4. This figure shows that although the Corcos model does a good job of matching the spanwise pressures, it fails to capture the “ridge” on the negative wavenumber side of the wavenumber-frequency spectrum for streamwise pressures. This ridge represents an upstream-propagating component of pressure. The authors found this discrepancy initially concerning, but Yang *et al.* (2017) showed that the Corcos model was still able to predict RMS structural accelerations within 3 dB of measured values for shocked runs. This margin of error is roughly equivalent to the same error found when the measured data was used directly to predict structural responses. The relative insensitivity of structural response to this difference in pressures is due to the fact that the structural response is based on the product of the wavenumber transforms of the pressure loading and structural mode shapes (see section 3.2). Since the mode shapes of the structure are independent of the direction of the flow (i.e., the structural waves are identical in either direction), the wavenumber transform of the structural mode shapes will be symmetric about  $K_x = 0$  and  $K_z = 0$ , and the predicted response is also independent of the sign of the pressure wavenumber. In other words, the same structural response would be predicted if the ridge on the negative wavenumber side shown in Fig. 4(a) were symmetrically moved across  $K_x = 0$  so that all of the energy is on the positive wavenumber side.

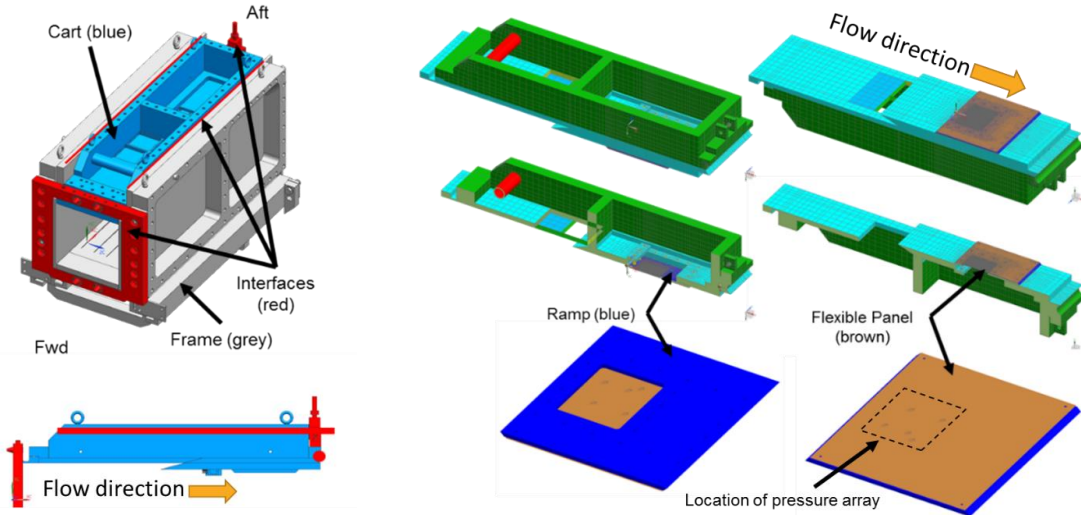


Fig. 3 Views of CAD model (left) and FEM (right)

This would yield a ridge on the positive wavenumber side similar to the Corcos model shown in Fig. 4(b).

Finally, the Corcos model is widely used in the aerospace community because it is familiar and easy to implement with existing tools. Since the authors’ goals are to provide some practical recommendations to practicing aerospace engineers, the decision was made to use the Corcos model for both unshocked and shocked data sets.

### 3.2 Prediction of structural response using wavenumber analysis

A finite element model (FEM) was created for the flexible panel part. It was originally used to correlate predicted panel responses to those measured in the wind tunnel, and therefore it represents all connected structures, up to and including the interfaces with the working section of the test tunnel. The left side of Fig. 5 shows a CAD model of the test article, with the modeled components shown in blue. The right side of the figure shows several views of the FEM created from the CAD. An assumed damping of 3% of critical damping was used for all frequencies.

The acceleration response of the panel was predicted using wavenumber analysis, which consists of two fast Fourier transforms: the first is a one-dimensional transform that converts time data to the frequency domain, and the second is a two-dimension transform that converts data in space to the wavenumber domain. The derivation for the acceleration response in  $G^2/Hz$  at a single location  $\mathbf{x}_0$  is expressed in Eq. (5), where  $g$  is the gravitational constant,  $f_r$  is the natural frequency of the  $r$ th mode, and  $\eta_r$  is the damping loss factor of the  $r$ th mode. The derivation of this equation is shown by Yang *et al.* (2017).

$$G_{aa}(\mathbf{x}_0, f) = \frac{(f)^4}{g^2} \sum_r \frac{\psi_r^2(\mathbf{x}_0) \hat{S}_{ff,r}(f)}{m_r^2 |f_r^2(1 + j\eta_r) - f^2|^2} \tag{5}$$

The panel’s response is a function of the displacement mode shape  $\psi_r$ , the modal mass of each mode  $m_r$ , and the modal force spectral density  $\hat{S}_{ff,r}$ , which describes how strongly each mode is

driven by the SFP. Hwang and Maidanik (1990) show that the modal force spectral density is calculated by integrating over the product of the wavenumber transforms of the SFP,  $\hat{\Phi}_{pp}$ , and vibration mode shapes,  $\hat{\Psi}$ . In practice, this is implemented as a summation over the wavenumber domain instead of an integral, as shown in Eq. (6), with  $N_x$  and  $N_z$  being the number of points in the  $k_x$  and  $k_z$  domains, respectively.

$$\hat{S}_{ff,r}(f) = \sum_{i=1}^{N_x} \sum_{j=1}^{N_z} \hat{\Phi}_{pp}(k_{x_i}, k_{z_j}, f) \left| \hat{\Psi}_r(k_{x_i}, k_{z_j}) \right|^2 \Delta k_x \Delta k_z \quad (6)$$

Note that Eq. (5) assumes that the individual structural modes are decoupled from each other, i.e., that the response of each mode can be individually calculated and then root-sum-squared to achieve an acceleration PSD response. In the authors' experience, this assumption of modal decoupling appears to be valid for a large number of cases.

#### 4. Description of methodology for sensor placement study

The purpose of this study was to provide recommendations for pressure sensor placement for transonic flows for both shocked and unshocked runs, relative to geometry (the top of the ramp) or flow features (the shock). The study was performed by selecting a small number of sensors from the pressure array shown in Fig. 2, using the experimentally measured pressures from the selected sensors to calculate Corcos auto- and cross-spectral coefficients, and then predicting the acceleration response of the panel with wavenumber analysis.

This study focused on the location of streamline sensors and does not provide recommendations for placement of spanwise sensors, due to the lack of spanwise sensors at large numbers of streamwise locations; Fig. 2 shows that closely spaced spanwise sensors exist at only three stations ( $x/h = 5.375, 8.0, 10.5$ ). The recommended Corcos-based model from Yang *et al.* (2017) was used for the spanwise decay coefficient. In that work, the spanwise decay coefficient is defined as a function of Strouhal number,  $St = fh/U$ , and two constants  $C1$  and  $C2$ , as given in Eq. (7). The values of these constants for unshocked flows are  $C1 = 0.34$  and  $C2 = 0.07$ . For shocked flows, the constants are  $C1 = 0.66$  and  $C2 = 0.02$ . As described by Yang *et al.* (2017), these constants were derived by fitting the Corcos model to the average of all adjacent spanwise sensor pairs in the wavenumber-frequency domain. The fit was performed separately for all unshocked and shocked runs.

$$\alpha_z = \sqrt{\frac{(C1 \times St)^2 + C2^2}{St^2}} \quad (7)$$

Sensors were selected from the upstream ( $0^\circ$ ) and downstream ( $180^\circ$ ) configurations (Fig. 2) separately, with no sensor combination allowed to span the two configurations. This is because the single centered reference sensor was insufficient<sup>a</sup> to lock the phasing between the upstream and downstream configurations.

For each combination of sensor locations, a MATLAB script was used to recover the Corcos auto- and cross-spectral coefficients and calculate the PSD acceleration at the five accelerometer

<sup>a</sup> To properly phase-lock the different array configurations, multiple references would be required.

locations. These PSD acceleration responses were averaged at each frequency, and the GRMS acceleration was calculated from the averaged PSD. The study used an exhaustive search approach, wherein all possible combinations of sensor locations were evaluated. For two sensors, this yielded a total of 351 possible sensor combinations for each of the upstream and downstream configurations (or 702 combinations in total).

The truth model is the average GRMS response at the five accelerometer locations when the pressure data from all sensors for all four array orientations (Fig. 2) is used directly to calculate the response using wavenumber analysis. This synthesized truth model allowed the authors to remove effects such as errors in the FEM, damping, and flanking excitation paths in the wind tunnel.

### 5. Results

Fig. 6 shows  $\Delta C_p = P_{RMS}/Q$ , the nondimensional RMS pressure, as a function of distance from the top of the ramp ( $x/h = 0$ ) for different Mach and stagnation pressure values, where  $h$  is the ramp height,  $P_{RMS}$  is the RMS pressure and  $Q$  is the dynamic pressure. The figure shows that Mach 0.75 and 0.80 are unshocked runs, whereas Mach 0.85 and 0.89 produce shocks. The location of the shock moves downstream with increasing Mach number. There is also a special case where the shock moves farther downstream for the Mach 0.89,  $P_o = 20$  psia case. This shift was caused by a minor increase in Mach number during wind tunnel testing. The figure also shows that while the fluctuating pressure at the shock is very high, it drops off quickly away from the shock.

The first subsection describes errors in vibration response prediction when the pressure sensor locations are chosen randomly. The second subsection describes recommended locations for sensor pairs for both unshocked and shocked runs. The third subsection describes attempts to improve results for shocked runs by placing an additional sensor at the shock location.

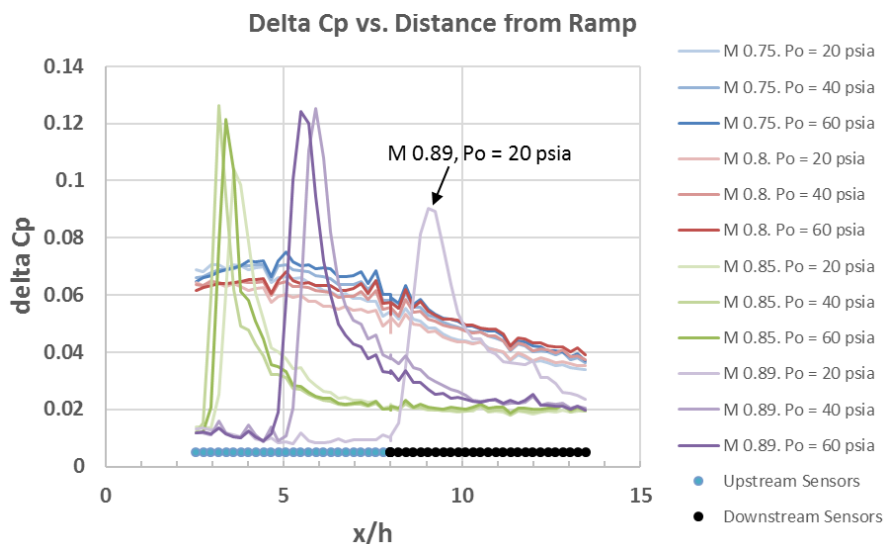


Fig. 4 Nondimensional RMS pressure versus distance from top of ramp, with locations of pressure sensors superimposed

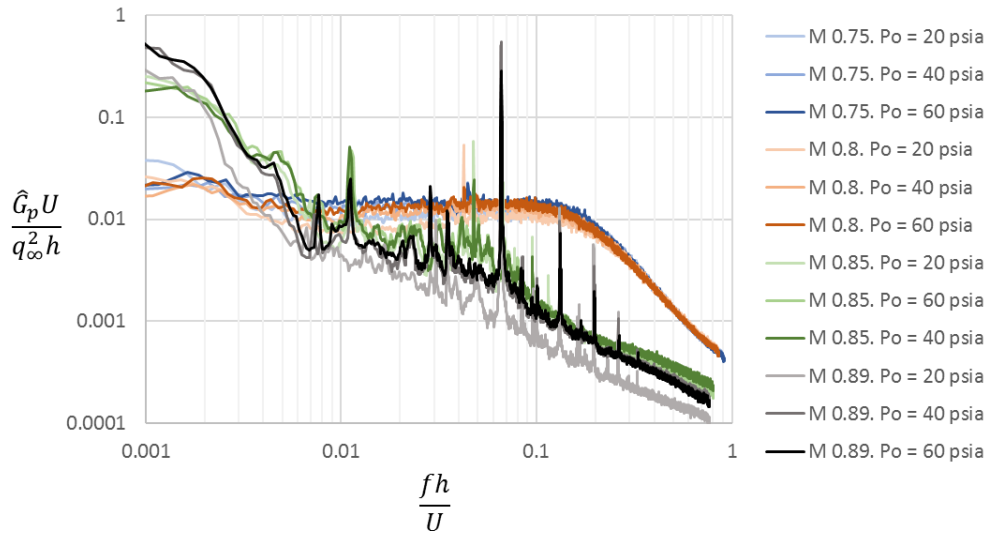


Fig. 5 Normalized spatially averaged pressure PSDs for all runs

The normalized<sup>b</sup> spatially averaged pressure power spectral densities (PSDs) are shown in Fig. 7. The PSD for the nonshocked runs (Mach 0.75, 0.80) is flat at low frequencies and then rolls off at high frequencies with a slope of  $(fh/U)^{-2}$ . The PSD for the shocked runs (Mach 0.85, 0.89) is dominated by low-frequency content and rolls at a lower frequency with a slope of  $(fh/U)^{-1}$ . The Mach 0.89 runs also contain a number of significant spikes in the data. These spikes were measured at all sensors and are believed to be a result of the normal shock interacting with the slots on the opposite side of the wind tunnel and exciting acoustic resonances in the tunnel. These pressure peaks cause narrowband acceleration peaks at the same frequencies that dominate the RMS response. As a result, the dominant excitation for the Mach 0.89 runs is not aeroacoustic in nature, and it cannot be assumed that the Corcos model is representative of the forcing function. Therefore, the majority of Mach 0.89 results are omitted from the remainder of the paper.

### 5.1 Errors in response prediction when sensor location is chosen randomly

To obtain some understanding of what errors should be expected if streamwise sensor pair locations are chosen randomly, the GRMS errors for all 702 possible location combinations were calculated at Mach 0.75, 0.80, and 0.85 for  $Po = 40$  psia. A histogram of the resulting errors is shown in Fig. 8, with a  $\pm 3$  dB error highlighted by the orange column. The figure shows that achieving less than 3 dB GRMS error would be possible only about 20% of the time.

Table 1 lists the mean and standard deviation of the absolute error for all four Mach values. The table shows that average errors are greater than 5 dB for runs without shocks. These errors increase to approximately 10 dB for Mach 0.85 that contains shocks. These results reinforce the need for proper placement of dynamic pressure sensors.

<sup>b</sup> Strouhal is based on the height of the ramp. Attempts were made to use boundary layer thickness or boundary layer displacement thickness as the characteristic length, but ramp height resulted in the best collapse of the data.

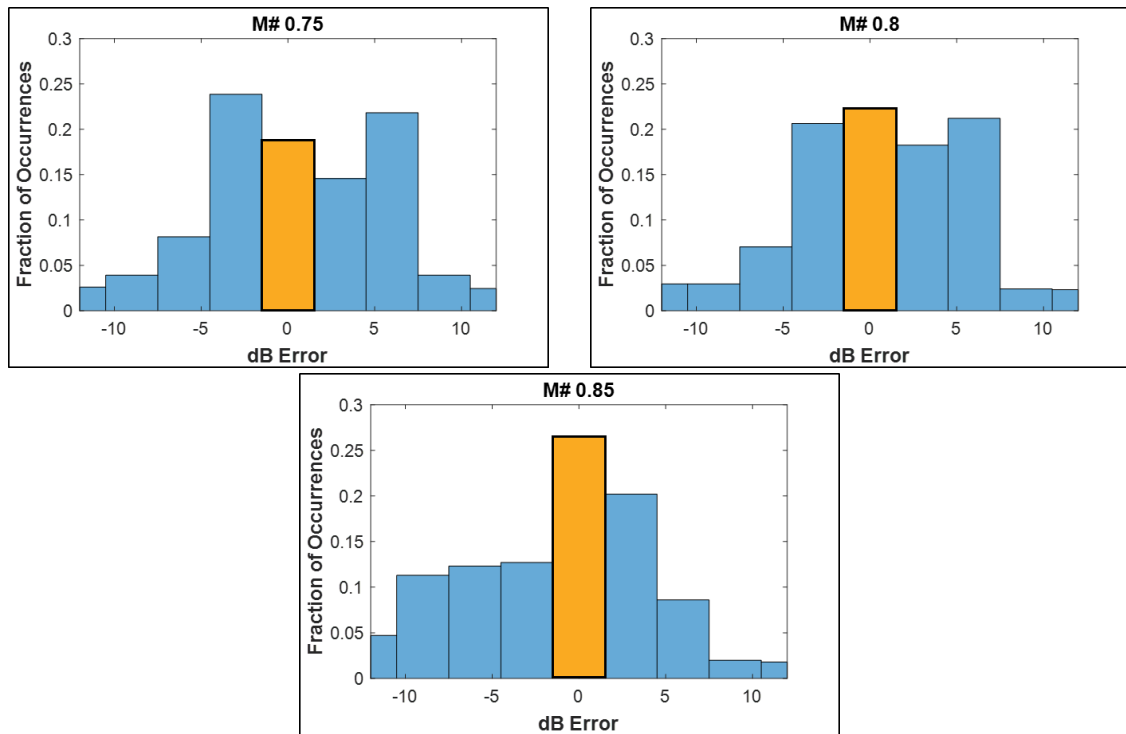


Fig. 6 Histograms showing less than 3 dB RMS error achieved only ~20% of the time if sensor location is chosen randomly

Table 1 Average and standard deviation of error when sensor pairs are placed randomly

Mach	Shock Exists?	Average Absolute Error (dB)	Standard Deviation of Error (dB)
0.75	No	5.6	7.7
0.80	No	5.1	7.1
0.85	Yes	9.7	12.3

### 5.2 Recommended placement with two sensors

This section discusses the results obtained when an exhaustive search of sensor locations was performed for two streamwise sensors. Recommendations for sensor placement are provided.

For each sensor location combination, the GRMS spatially averaged response was calculated and compared against the truth model. A contour map showing the absolute value of the GRMS error was then created, showing the error in structural response predictions for different sensor locations. An example in Fig. 9 shows the error for Mach 0.75 and Mach 0.80 at  $P_o = 40$  psia. In the figure, blue cells are sensor location combinations that result in low GRMS error. All possible sensor location combinations are shown by two right triangles: one for the upstream array configuration and one for the downstream array configuration. This allows the reader to visualize trends and extrapolate to sensor combinations that may not have been explicitly measured. The white square region in the upper right of each plot represents sensor combinations that span the array configurations and therefore cannot be directly evaluated. As indicated by the colorbar, blue

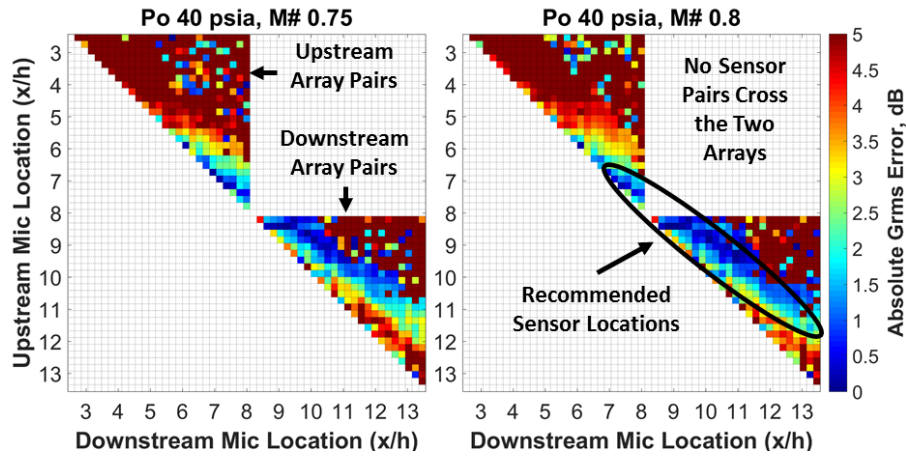


Fig. 7 Absolute GRMS error for two sensors for Mach 0.75,  $P_o = 40$  psia (left) and Mach 0.80,  $P_o = 40$  psia (right), showing both upstream and downstream array orientations

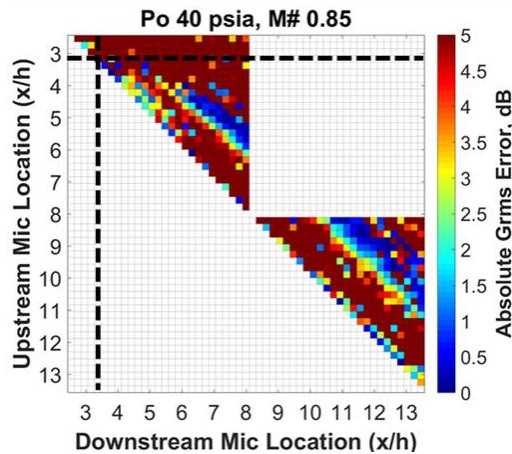


Fig. 10 Absolute GRMS error for two sensors for Mach 0.85,  $P_o = 40$  psia showing both upstream and downstream array orientations. Shock location is indicated with dashed line

regions represent sensor locations resulting in low GRMS error, and dark red regions represent high GRMS error. In each right-triangular region, the sensor pairs are spaced close together in regions near the diagonal of the contour plot, and the distance between sensors grows for regions near the top right of the plot. Changes in stagnation pressure did not significantly affect the contour plots; therefore, for sake of brevity, only plots for a single stagnation pressure are shown.

Fig. 9 shows that the contours for Mach 0.80 are very similar to those for Mach 0.75, which indicates that the recommended sensor locations are consistent for unshocked runs at both Mach numbers. More specifically, streamwise sensor pairs should be placed at least 6.5 ramp heights downstream of the ramp. Fig. 10 shows the GRMS error contours the shocked case at Mach 0.85,  $P_o = 40$  psia. This figure indicates that sensors should generally be placed downstream and away from the shock location. Unfortunately, only data for a single shock location is available, so it is difficult to provide guidance for cases where the shock has moved further aft on the flexible panel.

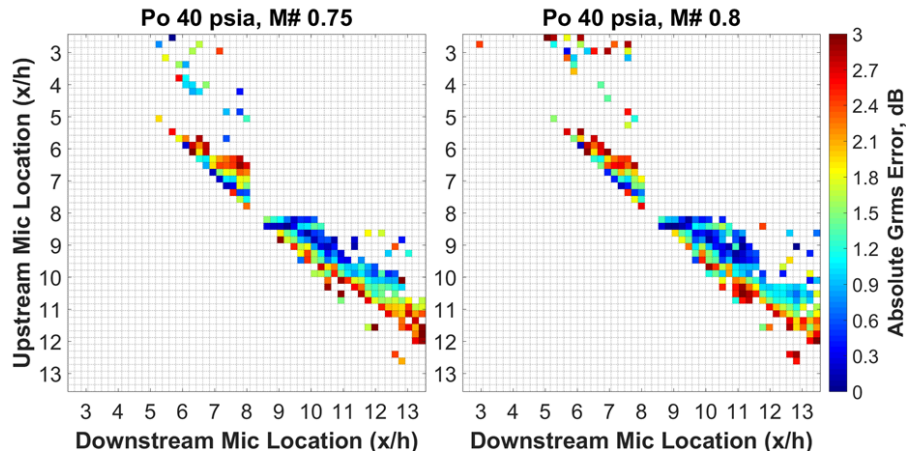


Fig. 8 Absolute GRMS error for two sensors with filter applied for Mach 0.75,  $P_o = 40$  psia (left) and Mach 0.80,  $P_o = 40$  psia (right)

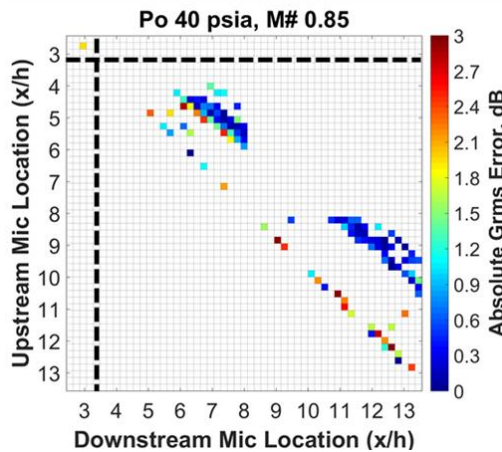


Fig. 9 Absolute GRMS error for two sensors with filter applied for Mach 0.85,  $P_o = 40$

This is explored in greater detail later in this paper.

The predicted GRMS response is a function of the combined effects of the auto- and cross-spectral parameters of the Corcos model. Therefore, it is possible for errors in one parameter to be offset by errors in a different parameter, resulting in location recommendations with low GRMS error despite large errors in one or more parameters. In an effort to remove these false positives, a filter was used to remove all sensor location combinations that did not yield average RMS pressures within 3 dB of the truth model, GRMS responses within 3 dB of the truth model, and a  $U_c/U_o$  ratio within 0.2 of the truth model, where  $U_o$  is the freestream velocity.

Fig. 11 shows the filtered results for the unshocked runs (Mach 0.75 and 0.80). The maximum value of the colorbar has been changed to 3 dB, so all colored locations in these figures can be considered to be reasonable suggestions for sensor placement.

Filtered sensor locations for the shocked run at Mach 0.85 at 40 psia are shown in Fig. 12. The recommended sensor locations begin at least a ramp height downstream from the shock. These

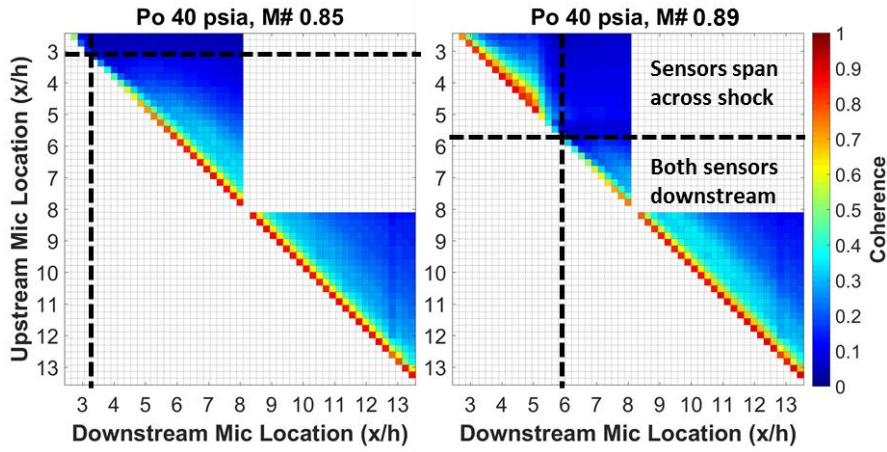


Fig. 10 Average coherence across all frequencies for sensor pairs for shocked runs, Mach 0.85, Po = 40 psia (left) and Mach 0.89, Po = 40 psia (right). Shock location indicated by dashed line

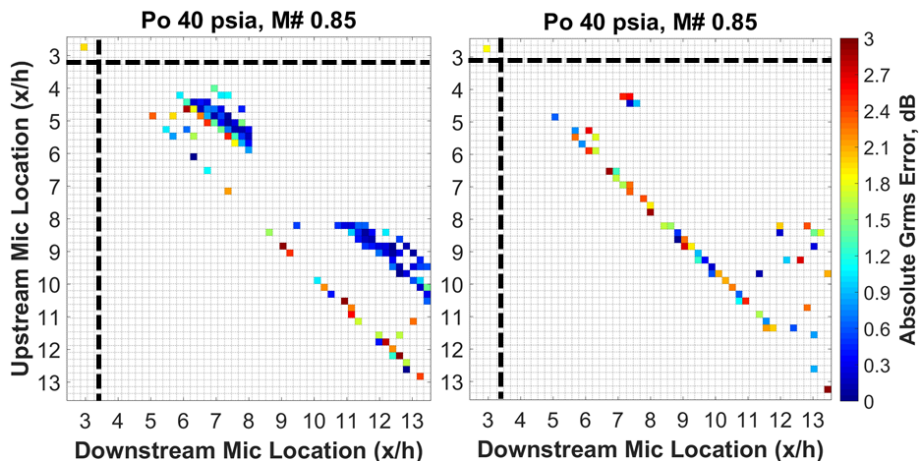


Fig. 11 Absolute GRMS error with filter applied for Mach 0.85, Po = 40 psia. Two sensor locations (left) and two sensor locations with spatially averaged pressure auto-spectrum including additional sensor under shock (right)

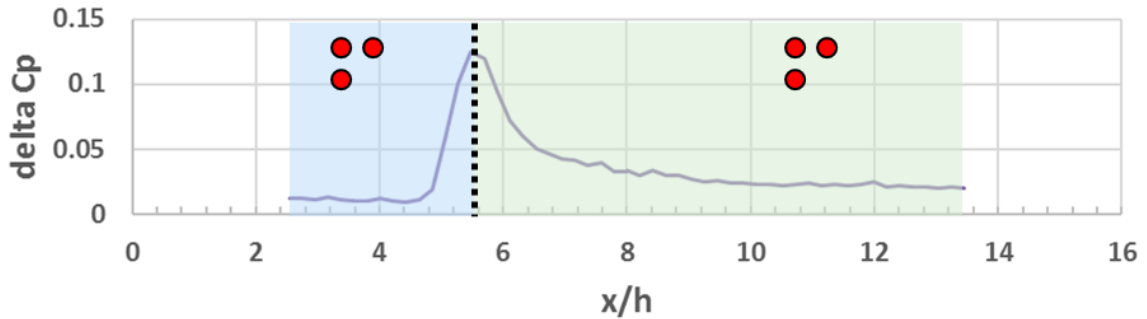


Fig. 12 Notional illustration of the shock to create two separate loading zones. Red circles indicate potential microphone locations

locations likely work because (1) this region is well aft of the shock, so the Corcos model is more likely to be a reasonable representation of more homogeneous surface pressures, and (2) the average autospectra of sensors in this region are more likely to match the area-averaged autospectra of all sensors, as indicated by Fig. 6.

Fig. 13 shows the coherence averaged across all frequencies for Mach 0.85 and 0.89. As expected, the coherence tends to be higher for sensors that are close together and lower for sensors that are farther apart. However, the average coherence drops to near zero in the vicinity of the shock and also for sensor pairs that span the shock. This indicates that the shock serves as a total “reset” of the turbulent boundary layer and that no coherent flow structures can pass through the shock. If this is the case, a shock location could be used to define the boundary between SFP loading zones since there would thus be no correlation from one zone to the next.

### *5.3 Adding additional sensor for shocked runs*

Up to this point, this study focused on making location recommendations for a single streamwise pair of sensors. In practice, there may be instances where additional sensors could be allocated to the region of interest; an additional sensor could be placed directly under the shock to capture the elevated SFP levels at that location.

To evaluate this possibility, an additional analysis was performed wherein the cross-spectral parameters from the original two-sensor pairs were used, but the spatially averaged pressure autospectrum now included the SFP from an additional sensor located directly under the shock. The results of this study are shown in Fig.14 . Overall, the inclusion of this additional sensor under the shock appears to degrade the predictions. Although there is a small improvement for adjacent sensor pairs along the diagonal, the larger regions of acceptable locations have disappeared.

The authors speculate that SFP measurements for a shock would best be performed by splitting the measurements (and therefore pressure loading) into two zones, with zone 1 being the region upstream of the shock and zone 2 being the region downstream of the shock. This is notionally illustrated in Fig. 15. Zone 2 sensor placement can use Fig. 12 as a guide. Zone 1 sensor placement will require further study. Note that the fluctuating pressures aft of the shock are higher. Therefore, the panel response could be dominated by fluctuating pressures in zone 2, provided the area of zone 2 is equivalent to or larger than the area of zone 1.

## **6. Conclusions**

A wind tunnel test was conducted that measured the SFP on the surface aft of a ramp at transonic speeds. SFP data from this test was used to perform a study to determine the best location for streamwise sensor pairs for shocked and unshocked runs based on minimizing the RMS acceleration response of a panel. Data at two Mach numbers were available for the unshocked runs, whereas data at only a single Mach number was available for the shocked run, due to the presence of large nonaeroacoustic tonal peaks at Mach 0.89 that dominated the RMS panel response. An analysis of the errors in response prediction when the sensor location is chosen randomly revealed that achieving less than 3 dB GRMS error would be possible only about 20% of the time.

The recommended locations for pressure sensors are summarized in Table 2. For unshocked conditions, the upstream sensor is best placed at least 6.5 ramp heights downstream of the ramp,

Table 2 Recommendations for sensor placement, with  $h$  indicating ramp height

Flow Type	Upstream Sensor	Downstream Sensor
No shock	> 6.5 $h$ from corner	< 2 $h$ from other sensor
Shocked	1–7 $h$ downstream from shock	2–3 $h$ from other sensor

and the downstream sensor should be within 2 ramp heights from the upstream sensor. The authors believe that this region is downstream of the separation region immediately aft of the ramp. Since the separation region occurs over a relatively small region of the panel, locating the sensors downstream provides the best chance for measuring auto-spectra matching the area-averaged autospectra over the panel. The close proximity of the second sensor represents the need to measure the coherence between the two sensors before the coherence has dropped to near zero.

For shocked conditions, the upstream sensor should be between 1 and 7 ramp heights downstream of the shock, with the downstream sensor 2 to 3 ramp heights of the upstream sensor. This recommendation is somewhat limited because it relies on one data set where the shock is located near the upstream end of the region of interest so that the majority of the flexible panel was in a region downstream of the shock. Therefore, the recommendation may be limited to cases where the vibration zone of interest is similarly largely aft of a shock.

The shock prevents coherent flow structures from being transmitted through the shock; therefore, measurements may need to be taken in multiple subzones relative to the shock location as the shock moves downstream. Attempts to supplement sensor pairs with an additional sensor near the shock resulted in larger errors.

As a practical matter, a wind tunnel test engineer does not have the luxury of placing sensors at different locations for the variety of flow conditions expected during test. However, the engineer can make use of steady CFD analysis to estimate shock locations and try to select locations that suit both shocked and unshocked runs. If the sensor budget permits, additional sensors can be placed to suit specific flow conditions, and data from only the appropriate sensor locations would be used after testing to define the loading environments.

## Acknowledgments

The wind tunnel design, operation, and data collection were funded by NASA under contract number NNX15CM16C. The authors wish to thank John Wilby for his advice and valuable feedback.

## References

- Alter, S.J., Brauckmann, G.J., Kleb B., Glass, C.E., Streett, C.L. and Schuster, D.M. (2015), "Time-accurate unsteady pressure loads simulated for the space launch system at wind tunnel conditions", *Proceedings of the 33rd AIAA Applied Aerodynamics Conference*, Dallas, Texas, U.S.A., June.
- Coe, C.F. and Chyu, W.J. (1972), "Pressure-fluctuation inputs and response of panels underlying attached and separated supersonic turbulent boundary layers", NASA TM X-62189.
- Corcos, G.M. (1963), "Resolution of pressure in turbulence", *J. Acoust. Soc. Am.*, **35**(2), 192-199. <https://doi.org/10.1121/1.1918431>.
- Hwang, Y.F. and Maidanik, G. (1990), "A wavenumber analysis of the coupling of a structural mode and

- flow turbulence”, *J. Sound Vib.*, **142**(1), 135-152. [https://doi.org/10.1016/0022-460X\(90\)90587-P](https://doi.org/10.1016/0022-460X(90)90587-P).
- Murray, N.E., Jansen, B.J., Yang, M.Y. and Palodichuk, M.T. (2017), “Measurements of surface pressure fluctuations and flexible panel response to a transonic reattaching flow”, *Proceedings of the 23rd AIAA/CEAS Aeroacoustics Conference*, Denver, Colorado, U.S.A., June.
- Reed, D.K., Mayle, M.N. and Nancy, D.K. (2012), “Comparison of Ares I-X flight and wind-tunnel aeroacoustic data”, *J. Spacecraft Rockets*, **49**(4), 659-665. <https://doi.org/10.2514/1.A32181>.
- Rizzi, S.A., Rackl, R.G. and Andrianov, E.V. (2000), “Flight test measurements from the Tu-144LL structure/cabin noise follow-on experiment”, NASA/TM-2000-209859.
- Yang, M.Y., Palodichuk, M.T., Murray, N.E. and Jansen, B.J. (2017), “Prediction of structural response in transonic flow using wavenumber decomposition of fluctuating pressures”, *Proceedings of the 23rd AIAA/CEAS Aeroacoustics Conference*, Denver, Colorado, U.S.A., June.
- Yang, M.Y. and Palodichuk, M.T. (2018), “Recommendations on dynamic pressure sensor placement for transonic wind tunnel tests”, *Proceedings of the Noise and Vibration Emerging Methods Conference*, Ibiza, Spain, May.